



Development, optimization and characterization of a two step sol–gel synthesis route for ZnO/SnO₂ nanocomposite

Isha Das¹ · Suresh Sagadevan¹ · Zaira Zaman Chowdhury² · Md. Enamul Hoque³

Received: 18 October 2017 / Accepted: 29 November 2017 / Published online: 7 December 2017
© Springer Science+Business Media, LLC, part of Springer Nature 2017

Abstract

In this research, two-step sol–gel synthesis method has been used to prepare coupled semiconductor metal oxide nanocomposites of SnO₂/ZnO. The structure and crystalline phase of the sample was identified using the X-ray powder diffraction analysis. The XRD pattern of SnO₂/ZnO nanocomposite exhibited all the diffraction peaks for both SnO₂ (tetragonal phase) and ZnO (hexagonal wurtzite phase). Surface morphological features of the prepared samples were analyzed using Scanning electronic microscopic analysis. Particle shape and size of the developed nanocomposite samples were analyzed using Transmission electronic microscopic analysis. Prepared nanoparticles have average particle size of 28 nm. EDX spectrum was used to obtain the elemental composition of the prepared sample. The peaks observed from EDX spectrum is analogous to all three elements (Sn, Zn and O) confirming the formation of SnO₂/ZnO nanoparticles. Raman spectroscopic analysis was carried out to observe the peak shift of the individual composite materials. The optical properties of the samples were examined using UV–Vis reflectance and photoluminescence spectroscopic analysis. The value of band gap of SnO₂/ZnO Nanocomposite was found to be 3.15 eV. The dielectric constant, dielectric loss and AC conductivity at different temperatures and frequencies were determined to obtain the typical dielectric behavior of the synthesized nanocomposite.

1 Introduction

The development of nanostructured metal oxide semiconductors has gained intense interest among the research community due to their versatile applications in different functional devices [1–3]. The unique physio-chemical properties including the high surface-to-volume ratios, optical and electrical properties enable the nano-structured metal oxides like TiO₂, ZnO, and SnO₂ to be considered extensively as high quality candidates for ultrasensitive and extremely miniaturized chemical sensors [4]. Semiconductor metal oxides are also used as photo-catalysts for effective elimination of

hazardous organic molecules from industrial waste effluents. However, its' large scale application is limited owing to its' rapid rate of recombination of the photo excited electron–hole pairs which is the crucial factor for efficient photo-degradation of organic molecules. Thus much effort has been given to upgrade its' synthesizing methods to lower the recombination tendency of electron–hole pairs which subsequently can enhance the photo-catalytic efficiency of the overall process. Tin oxide or stannic oxide (SnO₂) is considered as a promising semiconducting material for synthesizing hybrid nanocomposites as it can be potentially applied for development of next generation devices. SnO₂ can exhibit crystalline structure with rutile structure. It is an n-type semiconductor having a wide direct band gap energy of (3.6 eV) [5]. It can exhibit excellent optical properties with transparency and semi conductivity which can make it suitable for variety of practical applications including heat mirrors, cosmetic, drug-delivery carriers photo-catalysts, dye sensitized molecular sensors, glass melting electrodes, lithium ion batteries, conducting coatings, gas sensing materials and anti-reflecting coating in solar cells, etc [6–8]. Potential application of another semiconducting II–VI metal oxide such as ZnO is studied extensively. The wurtzite structure of zinc oxide (ZnO) is hexagonal and is

✉ Suresh Sagadevan
drsureshnano@gmail.com

✉ Zaira Zaman Chowdhury
dr.zaira.chowdhury76@gmail.com

¹ Centre for Nanotechnology, AMET University, Kanathur, Chennai 603 112, India

² Nanotechnology & Catalysis Research Centre, University of Malaya, 50603 Kuala Lumpur, Malaysia

³ Department of Biomedical Engineering, King Faisal University, Al-Hofuf, Al-Ahsa 31982, Kingdom of Saudi Arabia

frequently used as pigment, photo-catalysts, optical modulator wave guides, luminescence devices, dye sensitized solar cells, and light-emitting diodes etc [9, 10].

The band gap (E_g) values of ZnO and SnO₂ are 3.4 and 3.6 eV respectively. Thus these two metal oxides can be classified as the wide direct band gap semiconductor group [11, 12]. The wide band gap enables them to have good chemical and thermal stability under usual operating conditions. The width of the band gap of these nano-metal oxides can be varied to reduce the recombination of electron–hole pairs. Consequently, the photocatalytic activity of the solar cell can be improved [13]. Thus various investigations have been carried out to develop many combination techniques to obtain nanocomposites of ZnO and SnO₂ including co-precipitation, ball milling, partial solid state reduction and microemulsion [14–17]. Nevertheless, all these synthesis routes have unique advantage and disadvantage to obtain the final nano-material form. Incorporation of ZnO with SnO₂ can produce hybrid composites with eminent features of the individual constituent oxides with tunable characteristics based on user requirements. The ongoing research on this coupled oxide semiconductors is significant in tailoring the characteristics of next-generation sensors. There are different techniques, such as chemical vapor deposition (CVD) [18], physical vapor deposition (PVD), hydrothermal method [19], sol–gel method [20] etc., to synthesize the semiconductor hetero-structure materials exhibiting core–shell structure. However, the sol–gel route is considered as the easiest technique to scale up, feasible and less expensive. Sol–gel techniques have distinct advantage of preparing homogeneous composite aerogels with excellent compositional control and lower crystallization temperature. To date, very little research has been conducted to apply the sol–gel method to obtain ZnO/SnO₂ composites [21–24]. Previously Zn(CH₃COO)₂·2H₂O, oxalic acid and SnCl₂·2H₂O were used as starting materials and treated under 6 GPa pressure at to produce ZnO/SnO₂ composites [21]. Sol–gel and electro-spinning techniques were used consecutively to synthesize one-dimensional ZnO–SnO₂ nano-fibers [22]. Zinc acetate and SnCl₄ were dissolved in CH₃OH [24] or CH₃COCH₂COCH₃ and CH₃OC₂H₄OH [25] and dip coating sol–gel technique was carried out to prepare ZnO/SnO₂ thin films. Lately, another research group has reported the antibacterial performance of thin films produced from Zn (CH₃COO)₂·2H₂O, and SnCl₂·2H₂O dissolved in ethylene glycol and ethanol solutions, respectively [26]. The nanostructured SnO₂ and ZnO have shown high antibacterial properties. Thus, this nanocomposite can be used in chemical and biological sensors as well as in medical devices, dental composite materials, and textile materials to resist the bacterial growth up to a satisfactory level.

Based on synthesis routes and preparation condition, the structure and properties of the ZnO/SnO₂ nanocomposites

can be varied up to a greater scale to meet the consumer requirement and end usage of the final products. To the best of our knowledge, until now no research has been done to synthesize ZnO/SnO₂ nanocomposites using two step sol–gel process and thereby characterize the sample to analyze its' physiochemical as well as optoelectronic properties. Herein, a novel, two step, simple sol–gel method has been developed to synthesize the ZnO/SnO₂ nanocomposites whereby the process parameters were optimized to obtain insight about its' detailed characteristics. The prepared nano composite has been characterized by various physio-chemical and optoelectronic characterization techniques and are presented in subsequent sections.

2 Synthesis of SnO₂/ZnO nano-composite

The solvents and chemical reagents used here are analytical grade and they have been purchased and utilized without any further purification step. The two step sol–gel method was used here for the SnO₂/ZnO nanocomposite synthesis.

In brief, sol–gel synthesis, required amount of zinc sulphate heptahydrate (ZnSO₄·7H₂O) (28.75 gm) was added with distilled water to make the solution 1 M. At the same time, 0.015 M stannous chloride (SnCl₂) was prepared using distilled water (Solution A). 0.2 M aqueous solution of sodium hydroxide (NaOH) was prepared in another beaker (Solution B). Then, Tri-sodium citrate (Na₃C₆H₅O₇) (10 mg) was used as a capping agent and added to the above prepared solution 'B'. Finally, solution 'B' was added drop wise solution 'A' with vigorous stirring. The obtained solution color was changed from milky white to colourless. Overall the solution was stirred for 3 h. After the stirring had been stopped, then the solution was kept for another 30 min. At the bottom of the beaker, a white colored precipitate was formed. Hence, the precipitate thus obtained was washed with ethanol and distilled water for several times and dried. Finally, the samples were prepared, first by drying the precipitate in Hot air oven at about 70°C for 5 h.

2.1 Characterizations

The XRD pattern of the SnO₂/ZnO Nanocomposite was recorded by using a powder X-ray diffractometer Shimadzu model: XRD 6000 using CuK α ($\lambda = 0.154$ nm) radiation, with a diffraction angle between 20° and 80°. Scanning Electron Microscopy (SEM) studies were carried out on JEOL, JSM-67001. The samples needed a coating of gold for SEM analysis for the avoidance of charging effect. High resolution transmission electron microscope (HRTEM) image was taken using a JEOL 3010 with a UHR pole piece operates at an accelerating voltage 300 kV. Raman spectrum was collected using a Bruker RFS 27: stand-alone model Raman

spectrometer. Absorption spectrum was analyzed through the ELICO SL-159 UV–Vis conventional spectrophotometer in the range of 200–900 nm. The photoluminescence (PL) spectrum of the SnO_2/ZnO -nanocomposite was recorded using the Perkin–Elmer lambda 900 spectrophotometer with a Xe lamp as the excitation light source. The dielectric properties of the SnO_2/ZnO -nano-composite were analyzed

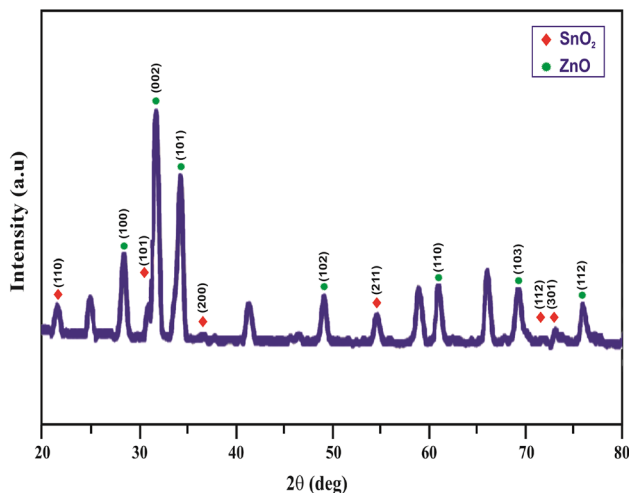
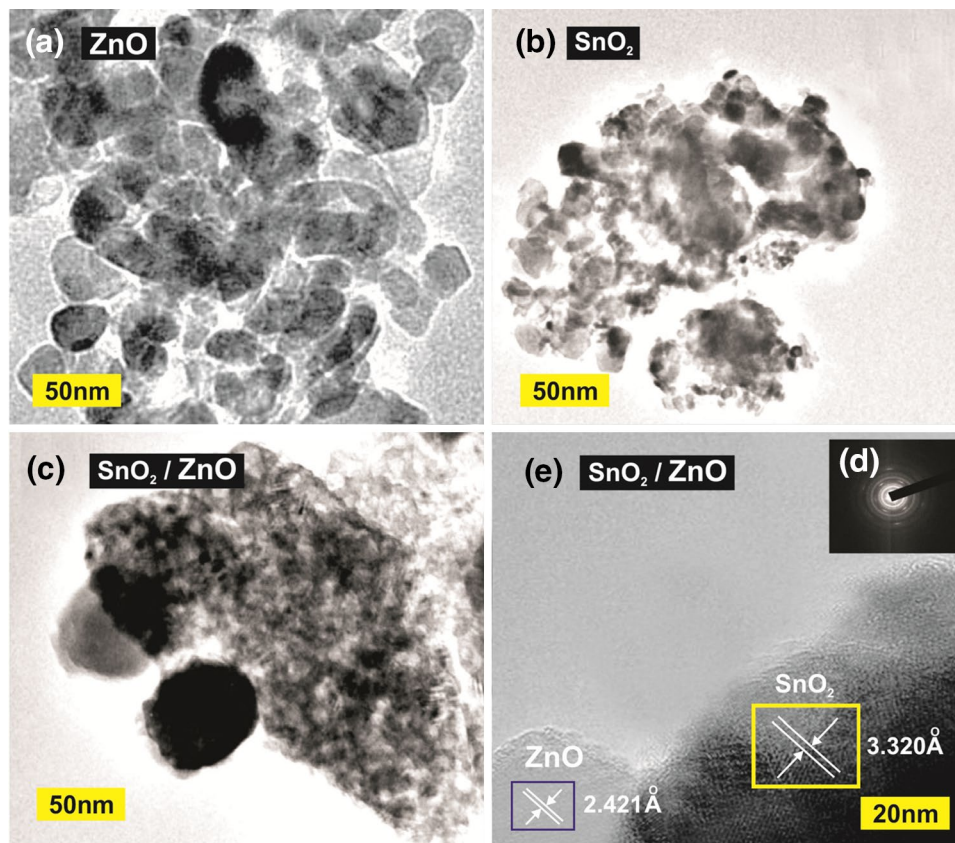


Fig. 1 XRD pattern of SnO_2/ZnO Nanocomposite

Fig. 2 TEM Images **a** ZnO, **b** SnO_2 , **c** SnO_2/ZnO , **d** SAED pattern, **e** HR-TEM SnO_2/ZnO



using an HIOKI 3532-50 LCR HITESTER over the frequency range 50 Hz–5 MHz.

3 Results and discussion

Fig. 1 illustrates the X-ray diffraction pattern of synthesized SnO_2/ZnO nanocomposite. The tetragonal structure of SnO_2 was confirmed by the presence of characteristic peaks around (1 1 0), (1 0 1), (2 0 0), (2 1 1), (1 1 2) and (3 0 1) planes. The hexagonal wurtzite structure of ZnO was evident from the diffraction peaks of the (1 0 0), (0 0 2), (1 0 1), (1 0 2), (1 1 0), (1 0 3), and (1 1 2) planes. The XRD pattern of SnO_2/ZnO nanocomposite exhibited all the diffraction peaks for both SnO_2 (tetragonal phase) and ZnO (hexagonal wurtzite phase). The phenomenon was further supported by SAED pattern analysis.

The particle size and morphology of the SnO_2/ZnO nanocomposite were observed using transmission electron microscopy (TEM) analysis and illustrated by **Fig. 2 a–c**. Prepared SnO_2/ZnO nanocomposite has average particle size of 28 nm. The SAED pattern obtained for SnO_2/ZnO nanocomposite is shown by **Fig. 2d**. The tetragonal structure of SnO_2 with (1 1 0), (1 0 1) and (2 0 0) planes, and the hexagonal wurtzite structure of ZnO with the (1 0 0) plane were confirmed by the diffraction rings of the SAED pattern.

The results were in agreement with the XRD analysis. This further confirms that ZnO shell formed here was polycrystalline and SnO₂ core nanoparticles have been formed.

The contrast shell and core of the particle in HR-TEM images suggest the core shell structure as shown in Fig. 2e. This is mainly due to the contribution of the different atomic numbers of SnO₂ and ZnO. It is evident from Fig. 2e that core/shell nanoparticles were confirmed during sol–gel synthesis process.

The surface texture with the elemental analysis of the SnO₂/ZnO Nanocomposite was carried out using scanning electron microscopy (SEM) and energy dispersive X-ray spectroscopy, respectively. Respective images of SEM and EDX patterns are illustrated by Fig. 3 a–d. The SEM images clearly reflected that highly porous nanograins were formed during the synthesis process. The SEM study reveals the formation of ZnO/SnO₂ nanocomposites via a cost effective Sol–gel method. These nanograins would increase the number of active sites to initiate adsorption of more oxygen species on the ZnO surface. This would subsequently facilitate to immobilize the gaseous molecules inside the pore channels. The peaks observed from EDX spectrum is analogous to all three elements (Sn, Zn and O) confirming the formation of SnO₂/ZnO nanoparticles.

The Raman spectrum obtained for SnO₂/ZnO Nanocomposites further confirms the XRD results and is demonstrated by Fig. 4. The peaks detected around 472 and

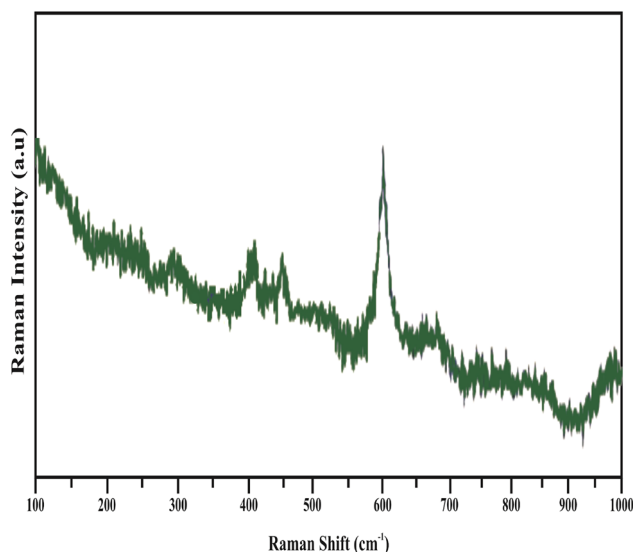
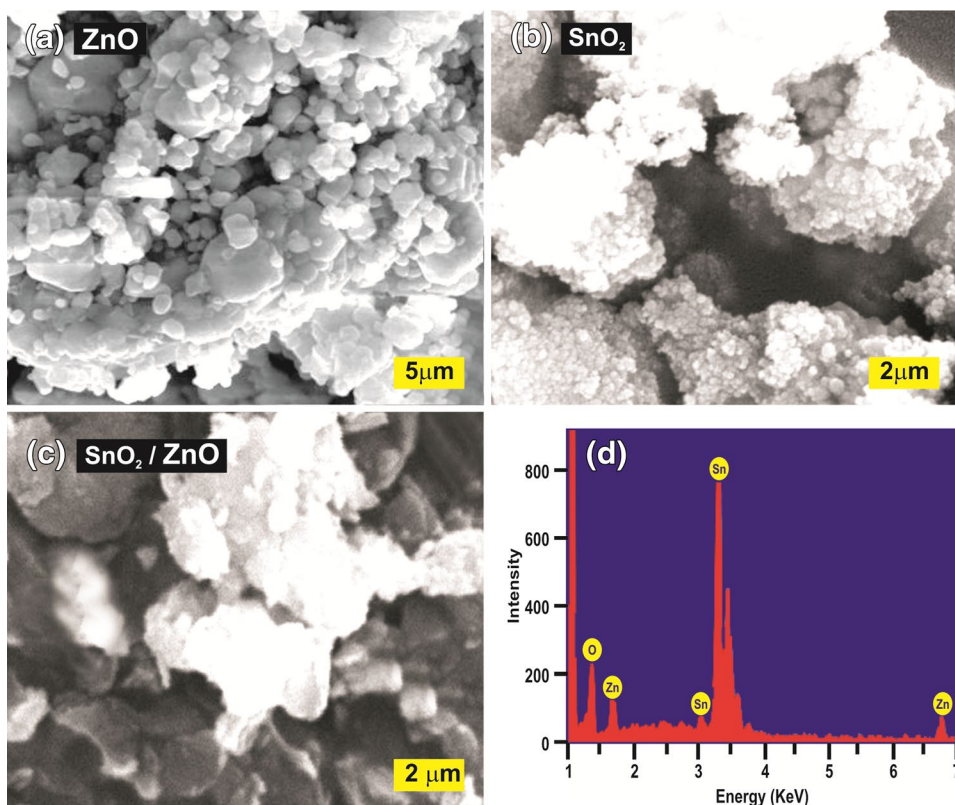


Fig. 4 Raman spectrum of SnO₂/ZnO Nanocomposite

636 cm⁻¹ are assigned to E_g mode and A_{1g} vibrational mode respectively. This further confirms the presence of the tetragonal structure of the prepared nanocomposite samples [27]. The Raman spectrum of ZnO nanoparticles shows the peaks equivalent to the modes at 332 cm⁻¹ which is ascribed for E₂ (high)–E₂ (low) modes. Another peak at 434 cm⁻¹ for ZnO nanoparticles is assigned to E₂ (high) mode. Presence

Fig. 3 SEM images a ZnO, b SnO₂, c SnO₂/ZnO and d EDX spectrum of SnO₂/ZnO Nanocomposite



of these peaks is representing the wurtzite crystal structure of ZnO [28]. All these characteristic peaks of SnO₂ and ZnO nanoparticles were shown by the Raman spectrum of the SnO₂/ZnO nanocomposites demonstrating no peak shift in the E_g and A_{1g} vibrational modes. The Raman spectrum of prepared nanocomposites exhibited no peaks with respect to the SnO₂-ZnO alloy.

The UV-Vis absorption spectrum for the prepared nanocomposites is presented by Fig. 5a. The maximum absorption in the spectrum is at 364 nm. ZnO presented the highest absorbance values in the UV region whilst SnO₂ revealed a low intensity absorbance due probably to its poor crystallinity. The absorbance of the mixed samples progressively decreased with increasing the content of SnO₂. The absorbance of the ZnO/SnO₂ nanocomposite has decreased. Higher absorbance provides a higher number of the absorbed photons and higher photocurrent. Therefore, the UV absorption spectrum has an abrupt absorption edge which is characteristic of a material with direct band gap energy.

The results revealed that, the magnitude of absorbance of the prepared composite was inversely proportional with the amount of SnO₂. Band gap (E_g) value was evaluated here by extrapolation of the linear part of the plots of $(\alpha h\nu)^2$ versus the energy of the exciting light and shown by Fig. 5b. The value of band gap of SnO₂/ZnO Nanocomposite was 3.15 eV. The band gap value obtained for the nanocomposite was relatively lower than the pure constituent oxides for the Zn/Sn molar ratio under investigation here. However the band gap energy calculated here was very close to that of pure ZnO which is evident due to addition of relatively lower amount of SnO₂.

The photoluminescence (PL) spectrum of prepared SnO₂/ZnO Nanocomposite is shown by Fig. 6. A narrow

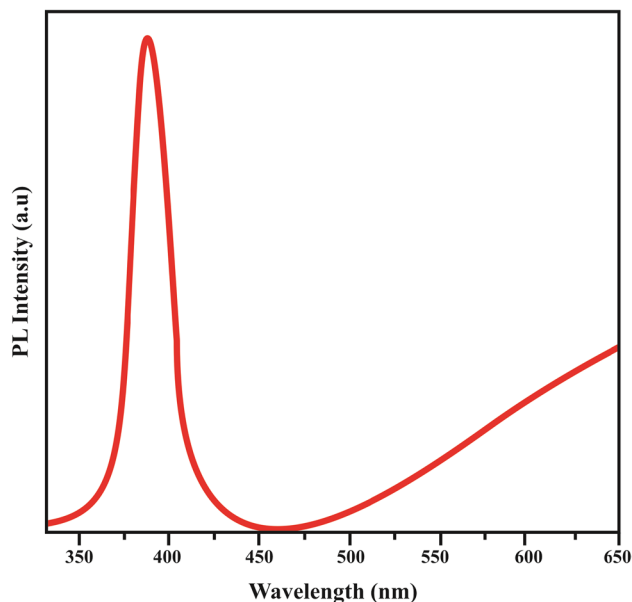


Fig. 6 Photoluminescence spectrum of SnO₂/ZnO Nanocomposite

ultraviolet peak at 380 nm was used to characterize the PL spectrum of ZnO nanoparticles. The results clearly demonstrated that coupling with SnO₂ had lowered the PL intensity of the prepared nanocomposite. Basically the radiative recombination of photogenerated electron-hole pair causes the Photoluminescence of the substrate. The photogenerated electrons migrate from the conduction band of ZnO to that of SnO₂, which would reduce the recombination of photoinduced electrons on the ZnO surface resulting the weakening the PL signal.

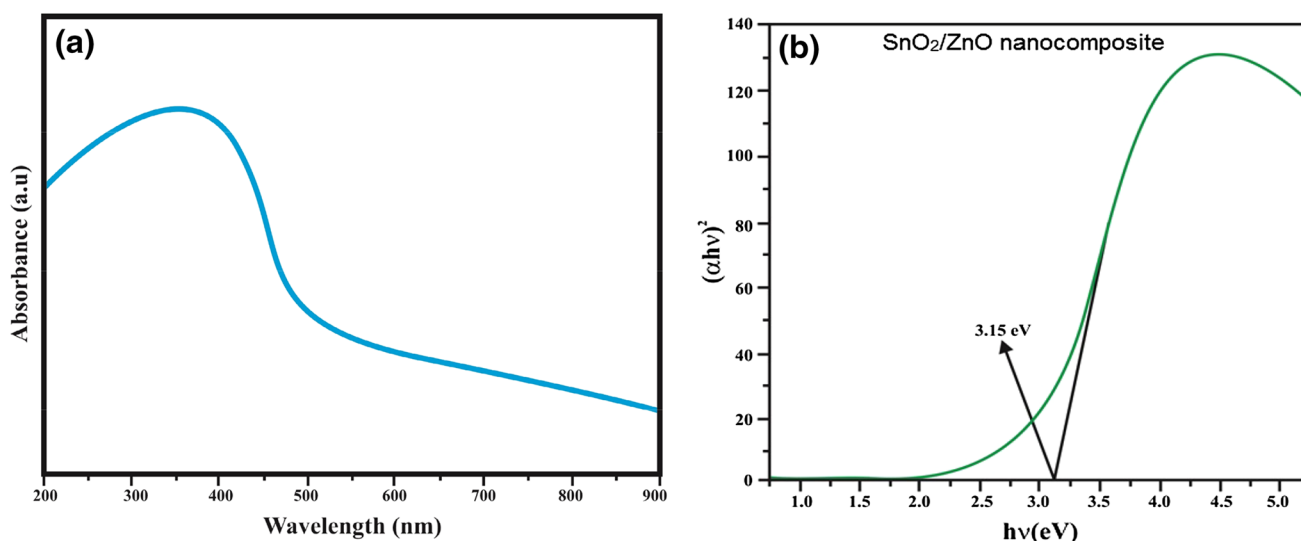


Fig. 5 **a** UV-Vis absorption spectrum of SnO₂/ZnO Nanocomposite, **b** plots of $(\alpha h\nu)^2$ versus $h\nu$ of SnO₂/ZnO Nanocomposite

The dielectric constant was calculated by using the relation (1)

$$\epsilon_r = \frac{Cd}{\epsilon_0 A} \tag{1}$$

where d and A being the thickness and the area of the specimen separately. The frequency has been varied from 5 Hz to 50 MHz to estimate the frequency dependence of the composites at specific temperature. Thus the frequency dispersion dielectric constant variation obtained for the composite at three different temperatures is plotted in Fig. 7. The results showed that, the dielectric constant of the prepared sample decreased with increasing frequency and after certain limit, it reached to a constant value. Overall the phenomenon was frequency dependent and the dielectric constant was relatively more at low frequency level i.e. the magnitude of dielectric constant is inversely related to the frequency level [29].

The high dielectric constant may be characterized to high ion jump orientation effect and increased space charge effect exhibited by the nanoparticles. Most atoms in the nanocrystalline materials are present at the grain boundaries that become active electrically because of charge catching. At low frequency values, dipole moment can effortlessly follow the changes in electric field. The contribution towards the increment in dielectric constant occurs because of the space charge and rotation polarization, which takes place mostly at the interfaces. Thus, the dielectric constant of nanostructures materials should be higher when compared to other conventional materials. The reason for increased dielectric constant of nanocrystalline materials at high temperature of higher space charge polarization owing to the structure of their

grain limit interfaces. Similarly, at high temperature, sharp increase of the dielectric constant rules the dielectric loss at lower frequencies and temperatures. As the temperature goes higher, space charge and ion jump polarization decreases, thus leading to a dielectric constant reduction [30].

Figure 8 shows the dielectric loss as a function of frequency level at various temperatures under investigation. The magnitude of dielectric loss values reduced with increased frequency, following the identical trend like that of the dielectric constant. The dielectric loss was higher with increasing temperatures. The dielectric loss is also high at low frequency level and with elevated frequency; it dropped significantly [31]. With increasing temperature, the dielectric loss was increased. This further revealed the thermally activated characteristics of the dielectric relaxation of the composite system [32, 33].

Figure 9 illustrated that, the AC conductivity reaches to higher values with the increase in frequency level for all the temperature ranges studied here. This phenomenon is consistent and supported by other literature also [34]. The possible explanation behind this is the short range translational movement of charge carriers between the confined positions [35]. Since hopping of the electrons is accelerated at higher frequency level, the AC conductivity of the composite also increases [36]. With the elevated temperature, the grain size of the sample increases resulting the reduction in grain boundaries. For small polaron hopping, the AC conductivity is increasing with higher frequency.

The electrical conductivity exhibits minute increase in the nanomaterial at low frequency region for as the frequency increases and it remains the same at all temperatures. Conversely, at high frequency value, particularly in KHz, there occurs a rapid increase in the conductivity value

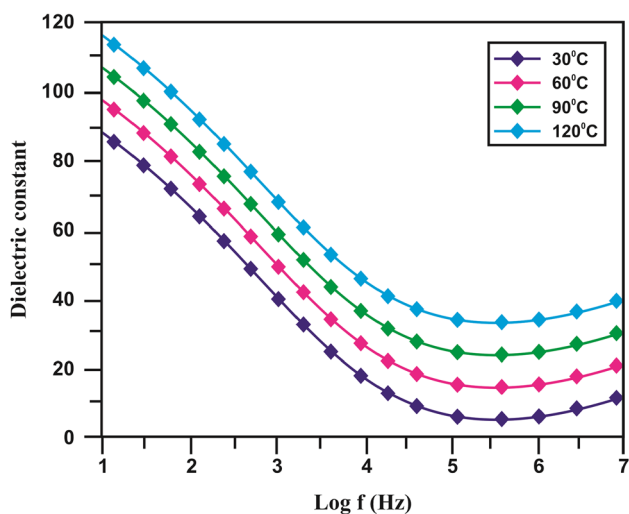


Fig. 7 Frequency dispersion dielectric constant variation of different temperature zone

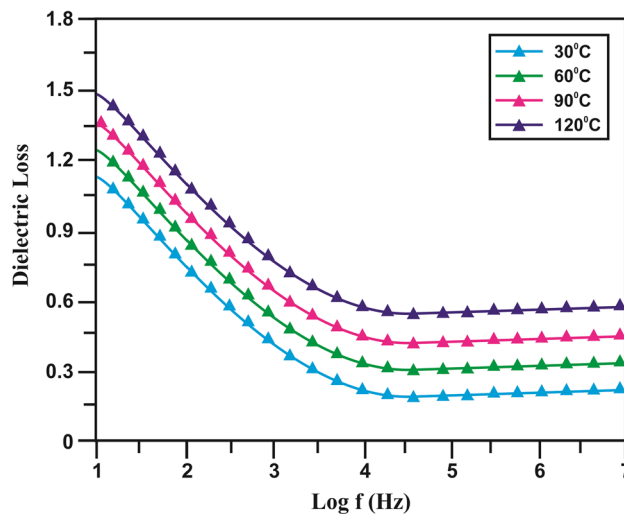


Fig. 8 Frequency dispersion dielectric loss variation within a certain temperatures zone

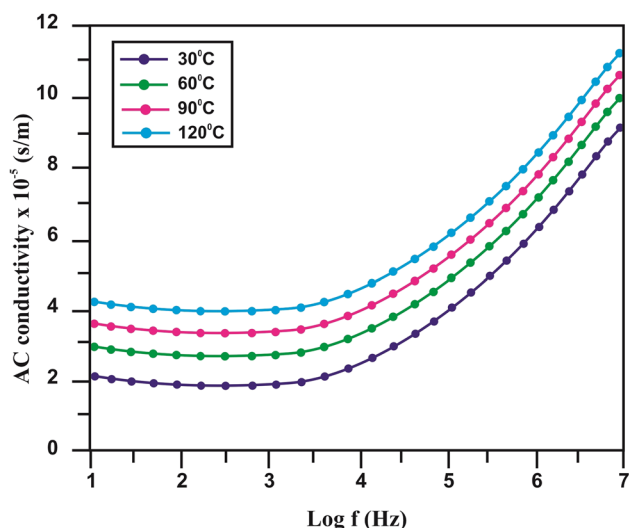


Fig. 9 AC conductivity plotted with different temperatures for SnO₂/ZnO nanocomposite

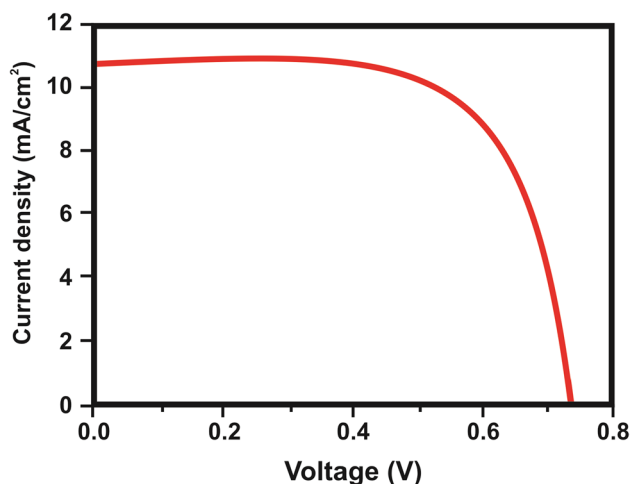


Fig. 10 J–V measurement of SnO₂/ZnO Nanoparticles

and it becomes enormous at high temperature which can be attributed to little polaron jumping [37]. At low frequency region, it is found that the frequency independent behavior that characterizes the DC conductivity and dispersion at higher frequency region exhibits the behavior of frequency dependence. It is consistent as the temperature increases resulting in a huge carrier hopping, which causes the conductivity to go higher.

The distinctive current density–voltage (J–V) curve of SnO₂/ZnO nanocomposite is illustrated by Fig. 10. The current density–voltage characteristics (J–V curve) are studied under standard solar light illumination. From the analysis of the J–V curves, critical parameters of the cell's operation are obtained. Open-circuit photovoltage (V_{oc}), short-circuit photo current density (J_{sc}), fill factor (FF), calculated using

Eq. (2), and the overall energy conversion efficiency (η), estimated by Eq. (3), are obtained.

$$EF = \frac{V_{max}J_{max}}{V_{oc}J_{sc}} \quad (2)$$

$$\eta = V_{oc}J_{sc}EF/I_s \quad (3)$$

where V_{max} and J_{max} are voltage and current densities for maximum power output, respectively. Whereas, I_s is the intensity of the incident light (mW/cm^2). ZnO–SnO₂ nanocomposite was coated on to ITO substrate. The coated substrates were heated at 470°C for 20 min. The current density–voltage (J–V) measurement was performed using light intensity of 10 mW cm^{-1} calibrated using Radiometer. The solar cell devices were fabricated with a weight ratio of 1:1 (SnO₂/ZnO) with an active layer concentration of 40 mg ml^{-1} for SnO₂/ZnO nanocomposite. The SnO₂/ZnO nanocomposite gives an efficiency of 3.12% with a J_{sc} value of 11.4 mA cm^{-2} , V_{oc} of 0.71 V and FF of 52%. The enhanced values of photocurrent density of the SnO₂/ZnO nanocomposite showed higher optical absorption capability and better separation of photogenerated electrons and holes [38]. The maximum open circuit photovoltage (V_{oc}) in SnO₂ was quite low (0.39 V) compared to pure ZnO (0.67 V) [39]. The trend for the magnitude of V_{oc} can be explained in terms of the position of the conduction band (CB) of the ZnO and SnO₂, respectively [40]. In particular, V_{oc} was 0.60 V, J_{sc} was $10.28 \text{ mA}/\text{cm}^2$ and FF was 57%. The power conversion efficiency (PCE) was 3.53%, i.e. about three times larger than for pure SnO₂ and three and a half time than pure ZnO as reported earlier in literature [39]. These results can be tentatively interpreted by observing the optimal position of ZnO conduction band, with respect to lowest energy unoccupied molecular orbital (LUMO) which in turn guarantees for V_{oc} enhancement, compared to pure SnO₂. The photocurrent was increased reflecting better transportation of electron, which is attributed to the tightly connected SnO₂ network. Polydispersion in sizes has been demonstrated to be extremely beneficial in ZnO-based DSSCs as it increases light capture and charge photogeneration. Similarly, a compact network is critical for electron transport, otherwise photogenerated charges tend to recombine when they are transporting towards the electrodes. The electrons collected are transported from ZnO to conductive substrate effectively via SnO₂ bridges thus suppressing the recombination. Furthermore, the high values of optical transparency of SnO₂ allow more sunlight passage to the dye molecules and enhance the light harvesting in the DSSCs. Also the findings demonstrated that, maximum part of the solar light remained unexploited in the ZnO-based DSSCs conversion. This enhances the photoconductivity leading to higher PCE. Additional studies are ongoing to evaluate the importance of SnO₂ incorporation using different ratios and

to determine the enhancement in the photovoltaic efficiency and performance of SnO₂/ZnO-nanocomposite.

4 Conclusions

In this work, a simple two step sol–gel synthesis technique has been developed to synthesize SnO₂/ZnO nanocomposite. The X-ray diffraction study ascertained the formation of synthesized SnO₂/ZnO nanocomposite. Raman spectrum confirmed strong peak existence due to SnO₂/ZnO nanocomposite. The SEM analysis confirmed the spherical shaped particles. The optical band gap value was about 3.15 eV and optical properties were studied. The detailed electrical analysis with frequency and temperature changes of the dielectric constant, the dielectric loss and AC conductivity of the prepared sample was investigated. The variation in dielectric constant and dielectric loss with respect to temperature and frequency dispersion has been analyzed for the prepared nano-composite material. These parameters showed decreasing trend with decreasing frequency level. Opposite trend was observed for these two parameters with increasing temperature. At higher temperature, the magnitude of frequency dependent AC conductivity indicated that the sample became thermally activated. The values of AC conductivity were increased with increasing temperature.

Funding Funding was provided by AMET UNIVERSITY(BKP-054-2015).

References

1. B. Tian, X. Zheng, T.J. Kempa, Y. Fang, N. Yu, G. Yu, J. Huang, C.M. Lieber, *Nature* **449**, 885 (2007)
2. W. Lu, C.M. Lieber, *Nat. Mater.* **6**, 841 (2007)
3. J.A. Rodriguez, M. Fernandez-Garcia, *Synthesis, Properties, and Applications of Oxide Nanomaterials*. (Wiley, New Jersey, 2007)
4. J.G. Lu, P. Chang, Z. Fan, *Mater. Sci. Eng. R* **52**, 49 (2006)
5. Z.Q. Liu, L.X. Ding, Z.L. Wang, Y.C. Mao, S.L. Xie, Y.M. Zhang, G.R. Lia, Y.X. Tong, *Cryst. Eng. Comm.* **14**, 2289 (2012)
6. X. Ma, J. Nanoeng. *Nanomanuf.* **2**, 143–149 (2012)
7. Y.J. Choi, I.S. Hwang, J.G. Park, K.J. Choi, J.H. Park, J.H. Lee, *Nanotechnology*, **19**, 095508 (2008)
8. B. Wang, L. Zhu, Y. Yang, N. Xu, G. Yang, *J. Phys. Chem. C* **112**, 6643–6647 (2008)
9. G. Singh, A. Choudhary, D. Haranath, A.G. Joshi, N. Singh, S. Singh, R. Pasricha, *Carbon* **50**, 385–394 (2012)
10. M. Carotta, A. Cervi, A. Fioravanti, S. Gherardi, A. Giberti, B. Vendemiati, D. Vincenzi, M. Sacerdoti, *Thin Solid Films* **520**, 939–946 (2011)
11. A. Alkaya, R. Kaplan, H. Canbolat, S.S. Hegedus, *Renew. Energy* **34**, 1595 (2009)
12. X. Song, Z. Wang, Y. Liu, C. Wang, L. Li, *Nanotechnology* **20**, 075501 (2009)
13. H. Wang, S. Baek, J. Lee, S. Lim, *Chem. Eng. J.* **146**, 355 (2009)
14. J.H. Yu, G.M. Choi, *Sens. Actuators B* **52**, 251 (1998)
15. Q. Kuang, Z.-Y. Jiang, Z.-X. Xie, S.-C. Lin, Z.-W. Lin, S.Y. Xie, R.-B. Huang, L.-S. Zheng, *J. Am. Chem. Soc.* **127**, 11777 (2005)
16. M. Zhang, G. Sheng, J. Fu, T. An, Z. Wang, X. Hu, *Mater. Lett.* **59**, 3641 (2005)
17. C. Liangyuan, B. Shouli, Z. Guojun, L. Dianqing, C. Aifan, C.C. Liu, *Sens. Actuators B* **134**, 360 (2008)
18. H.Y. Chao, S.H. You, J.Y. Lu, J.H. Cheng, Y.H. Chang, C.T. Liang, C.T. Wu, *J. Nanosci. Nanotechnol.* **11**, 2042–2046 (2011)
19. J. Jiang, H. Zhou, F. Zhang, T. Fan, D. Zhang, *Appl. Surf. Sci.* **368**, 309–315 (2016)
20. D. Li, X. Jiang, Y. Zhang, B. Zhang, C. Pan, *J. Mater. Res.* **28**(3), 507–512 (2013)
21. S. Zhenya, D. Yundi, Z. Weiyang, *J. Nanomater.* **2008**, 286069 (2008)
22. Z. Zhang, C. Shao, X. Li, L. Zhang, H. Xue, C. Wang, Y. Liu, *J. Phys. Chem. C* **114**, 7920–7925 (2010)
23. N. Talebian, M.R. Nilforoushan, E.B. Zargar, *Appl. Surf. Sci.* **258**, 547–555 (2011)
24. H. Uchiyama, R. Nagao, H. Kozuka, *J. Alloys Compd.* **554**, 122–126 (2013)
25. Z. Yang, L. Lv, Y. Dai, Z. Xv, D. Qian, *Appl. Surf. Sci.* **256**, 2898–2902 (2010)
26. D.Y. Torres Martínez, R. CastanedoPérez, G. Torres Delgado, O. ZelayaÁngel, *J. Photochem. Photobiol. A* **235**, 49–55 (2012)
27. K. Mcguire, Z.W. Pan, J. Menéndez, Z.L. Wang, A.M. Rao, D. Milkie, *J. Nanosci. Nanotechnol.* **2**, 5 (2002)
28. O. Lupan, T. Pauporte, L. Chow, *Turk. J. Phys.* **38**, 399–419 (2014)
29. S. Sagadevan, *Appl. Nanosci.* **4**, 325–329 (2014)
30. S. Sagadevan, K. Pal, *J. Mater. Sci.: Mater. Electron.* **28**, 9072–9080 (2017)
31. S. Sagadevan, K. Pal, P. Koteeswari, A. Subashini, *J. Mater. Sci.* **28**, 7892–7898 (2017)
32. K.A. Mangai, K.T. Selvi, M. Priya, M. Rathnakumari, P. Sureshkumar, S. Sagadevan, *J. Mater. Sci.* **28**, 2910–2922 (2017)
33. S. Sagadevan, I. Das, K. Pal, P. Murugasen, P. Singh, *J. Mater. Sci.* **28**, 5235–5243 (2017)
34. S. Suresh, C. Arunsheshan, *Appl. Nanosci.* **4**, 179 (2014)
35. M. Raghasudha, D. Ravinder, P. Veerasomaiah, *Mater. Sci. Appl.* **4**, 432 (2013)
36. S. Sagadevan, I. Das, P. Singh, J. Podder, *J. Mater. Sci.: Mater. Electron.* **28**, 1136–1141 (2017)
37. S. Sagadevan, J. Podder, *Int. J. Nanoparticles* **8**, 289–301 (2015)
38. I. Das, S. Sagadevan, Z.Z. Chowdhury, N. Vijayan, *J. Mater. Sci.: Mater. Electron.* (2017). <https://doi.org/10.1007/s10854-017-8070-4>
39. R. Milan, G.S. Selopal, M. Epifani, M.M. Natile, G. Sberveglieri, A. Vomiero, I. Concina, *Sci. Rep.* **5**, 14523 (2015). <https://doi.org/10.1038/srep14523>
40. J.A. Anta, E. Guillen, R. Tena-Zaera, *J. Phys. Chem. C* **116**, 11413–11425 (2012)